THE JOURNAL OF PHYSICAL CHEMISTRY C

pubs.acs.org/JPCC Article

Disclosing the Structural, Electronic, Magnetic, and Morphological Properties of $CuMnO_2$: A Unified Experimental and Theoretical Approach

A. A. G. Santiago,* R. L. Tranquilin, M. C. Oliveira, R. A. P. Ribeiro, S. R. de Lazaro, M. A. Correa, F. Bohn, E. Longo, F. V. Motta, and M. R. D. Bomio*

Cite This: J. Phys. Chem. C 2020, 124, 5378−5388 Read Online

ACCESS | Metrics & More | Article Recommendations | Supporting Information

ABSTRACT: Precise control of the overall performance for solid-state materials is associated with morphological modulations which provide an alternative way to the rational design based on understanding the corresponding electronic structures of the exposed surfaces. Experimental and theoretical efforts were combined herein to elucidate the structural−property relationship of $CuMnO_2$ nanoparticles from different morphologies. The microwave-assisted hydrothermal method was employed to synthesize these crystals with different morphologies, while first-principle quantum mechanical calculations were performed at the DFT level to obtain the structural, electronic, and magnetic properties of $CuMnO_2$ surfaces. Our structural results have confirmed a monoclinic structure for crednerite-type $CuMnO_2$ nanoparticles described by the Jahn−Teller-distorted octahedral $[MnO_6]$ clusters, which are connected by linear 2-fold $[CuO_2]$. FE-SEM images combined with Wulff construction analyses indicated that $CuMnO_2$ nanoparticles adopt a hexagonal nanoplate-like morphology which can enclose a major extent of the (100) surface with contributions from (101), (110), and (111) surfaces. Electronic structure and magnetic characterizations were discussed by the role of the corresponding electronic states of exposed surfaces which control the energy-level band diagram and spin density distribution. These results extend our fundamental understanding of the atomic processes which underpin the morphological modulations of the $CuMnO_2$ material, thus creating a new path to obtain selected nanoparticles with desirable properties which optimize their applications.

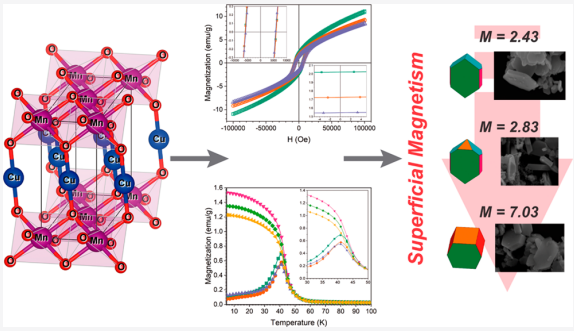

INTRODUCTION

Delafossite materials have attracted remarkable attention recently due to their potential applications as multiferroic, oxygen storage devices, photovoltaic and photocatalytic semiconductors, hydrogen photocathodes, and environmentally friendly platforms, among others.[1−10] This class of compounds can be described by a general formula ABO_2, with A and B being transition metal cations. The crystal structure usually consists of hexagonal delafossite, where the monovalent A^+ cations are linearly coordinated with two O ions and the parallel O−A−O chains connect edge-sharing $[BO]_6$ octahedrons formed by B^{3+} cations.[1]

$CuMnO_2$ material, called crednerite, is a very intriguing delafossite derivative which can be potentially applied in several fields such as catalyst, photoelectrochemical cells, and multiferroic devices, among others.[10−18] Regarding the crystalline structure, this material shows a distorted arrangement in comparison with the hexagonal delafossite structure because of the Jahn−Teller effect of Mn^{3+} ions. This cation has crystal-field splitting in e_g orbitals due to the $3d^4$ ($t_{2g}^3e_g^1$) electronic configuration. This fact lowers the trigonal symmetry to monoclinic ($C2/m$), having a significant effect on the magnetic arrangement of Mn^{3+} cations.[12,19] In this case, $CuMnO_2$ corresponds to an isosceles-triangular antiferromagnet (AFM), where the triangular *ab* plane is a nonequivalent plane, i.e., two short and four long Mn−Mn distances in the plane can be found for each Mn, resulting in a lift frustration associated with the strength of short (J_1) and long (J_2) antiferromagnetic exchange coupling involving Mn−O−Mn bond path interactions.[19,20]

In addition, an experimental evaluation of stoichiometric $CuMnO_2$ and nonstoichiometric $Cu(Mn_{1-x}Cu_x)O_2$ samples indicates that the in-plane magnetic ordering remains the same. However, there are changes to the interlayer exchange coupling

Received: January 8, 2020
Revised: February 13, 2020
Published: February 14, 2020

https://dx.doi.org/10.1021/acs.jpcc.0c00198
J. Phys. Chem. C 2020, 124, 5378−5388

from antiferromagnetic in pure $CuMnO_2$ to ferromagnetic (FEM) for $Cu(Mn_{1-x}Cu_x)O_2$ compositions, suggesting that long-range interlayer interactions play a fundamental role in controlling the magnetic properties of the crednerite structure.[21−23]

From an experimental point of view, a series of techniques has been employed to successfully synthesize the crednerite $CuMnO_2$, including solid-state reactions,[13−15,19,24] sol−gel techniques,[25,26] and hydrothermal methods.[11,12,27−30] The major releases associated with the power of the hydrothermal methods, as proposed in this work, are associated with a drastic reduction in synthesis temperature and time as well as the possibility to generate nanoparticles with controlled size and shape.[31] For instance, Fu et al. confirmed that hydrothermal methods can be used to tailor the $CuMnO_2$ morphology showing triangular sheets, nanowires, hexagonal prisms, and octahedron polyhedrons as a function of temperature.[11] This fact is mandatory to precisely control the overall properties of crednerite $CuMnO_2$ and could open new prospects in understanding the surface-induced properties such as intriguing magnetic properties due to the presence of uncompensated spins originated from the confinement quantum effect, as observed for other materials.[32,33]

Nevertheless, previously reported theoretical studies for $CuMnO_2$ have mainly been focused on understanding in-plane and out-of-plane magnetic ordering for both stoichiometric and nonstoichiometric compositions.[6,10,34] However, the global discussion on the connection between the electronic structure and the surface remains unclear. In this context, it is well known that a precise understanding of the semiconductor material morphology is critical to identify the correlations between crystalline structure, activity, and technological applications.[35−37] In particular, the strong dependence of the desirable properties with surface orientation can be understood from the viewpoint of singular chemical arrangement which arises from the exposed surfaces appearing in the morphology, resulting in intriguing influences on the surface electronic structure.[38]

On the basis of the above considerations, in this study we present a unified experimental and theoretical investigation to gather a comprehensive understanding of the solid-state chemistry in terms of the synthesis and properties for $CuMnO_2$. To do so, the energetic, structural, electronic, morphological, and magnetic properties of $CuMnO_2$ were analyzed by experimental techniques, with the major aspects being substantiated and further elucidated by state-of-the-art density functional theory (DFT) calculations. Our main insights are associated with the critical role of the single chemical environments found in the bulk as well as on surfaces of the $CuMnO_2$ material.

EXPERIMENTAL SECTION

Synthesis. Copper(II) nitrate hemi(pentahydrate) [$Cu(NO_3)_2{\cdot}2.5H_2O$] (Synth, 98% purity), manganese nitrate tetrahydrate [$Mn(NO_3)_2{\cdot}4H_2O$] (Synth, 99%), sodium hydroxide [NaOH] (Synth), and distilled water were used as reagents to synthesize the $CuMnO_2$ samples. The $CuMnO_2$ samples were prepared by the microwave-assisted hydrothermal method, as described in the literature.[12] The solution precursor for $CuMnO_2$ was composed by adding 6 mmol of $Cu(NO_3)_2$ and 6 mmol of $Mn(NO_3)_2$ into 30 mL of H_2O. Next, the pH solution was adjusted to 12 by adding NaOH (2.5 M), forming brownish precipitates, which was then stirred for 30 min. The solution was transferred and sealed in a Teflon autoclave and then heated by different temperatures and times under hydrothermal conditions with microwave radiation (2.45 GHz, maximum power 800 W, the heating rate of 30 °C/min), as shown in Table S1. The samples are named CM*T*-*t*, where *T* is the temperature and *t* is time utilized. The pressure inside the autoclave was stabilized at 4.0 bar. After heat treatment, the samples were washed with deionized water, centrifuged, and dried at 80 °C for 12 h.

Characterization. Powder X-ray diffraction (XRD) patterns for the $CuMnO_2$ samples were collected within the 10−120° angular range with a step speed of 0.02° min^{-1} using an XRD 7000 Shimadzu diffractometer and monochromatic Cu Kα (λ = 1.5406 Å) radiation. The diffraction patterns were analyzed by means of the General Structure Analysis System (GSAS) with the EXPGUI graphic interface[39] in order to perform the Rietveld refinement[40] and to analyze the possible structural modifications. The following parameters were refined: scaling factor and phase fraction; background (displaced Chebyshev polynomial function); peak shape (Thomson−Cox−Hasting pseudo-Voigt); change in the network constants; fractional atomic coordinates; and isotropic thermal parameters. Field-emission gun scanning electron microscopy (FESEM; Carl Zeiss, Supra 35-VP model, Germany, operated at 6 kV) was used to investigate the morphologies of the $CuMnO_2$ samples. A Shimadzu spectrophotometer (UV-2600 model) was utilized for measuring the ultraviolet−visible (UV−vis) reflectance mode of the samples. Magnetic characterization was performed with a Quantum Design Dynacool Physical Property Measurement System (PPMS). In this case, the zero-field-cooled (ZFC) and field-cooled (FC) magnetization curves were acquired in the temperature range between 5 and 300 K with a probe magnetic field of 500 Oe. Moreover, isothermal magnetization was measured with a magnetic field up to 100 kOe and after zero-field cooling at selected temperatures between 5 and 300 K.

Computational Details. DFT calculations in this study were performed within the linear combination of atomic orbitals (LCAO) approach, as implemented in the CRYSTAL17 code.[41] Cu, Mn, and O atoms were described by the atom-centered all-electron 86-4111d41G, 86-411d41G, and 8-411d1G Gaussian basis sets, respectively.[42−44] The B3LYP[45] hybrid functional was employed in all calculations for treating the exchange and correlation effects. Here, it is important to point out that Becke-based hybrid exchange correlation functionals were selected due to the good agreement between the calculated and the experimental band gaps of complex oxide materials.[46−50] The analyses of the electronic properties in terms of the density of states (DOS) projections, band structure profiles, and electronic density distributions were carried out with the new property evaluation functionalities available in the latest version of the CRYSTAL code.[41] The pristine monoclinic (*C*2/*m*) unit cell for $CuMnO_2$ was built using the experimental lattice parameters and atomic positions obtained from the Rietveld refinement. Lattice parameters and atomic positions were fully relaxed considering a FEM configuration. Two additional models were considered using a 2 × 2 × 1 supercell to investigate the exchange coupling constant along the nearest neighboring [MnO_6] clusters. The first model was described in antiferromagnetic (AFM-1) ordering corresponding to a supercell with two magnetic Mn^{3+} sites with parallel orientation (FEM) for the short Mn−O−Mn bond path, while the spin arrangement for Mn^{3+} sites

https://dx.doi.org/10.1021/acs.jpcc.0c00198
J. Phys. Chem. C 2020, 124, 5378−5388

along the longer Mn−O−Mn bond paths was oriented as AFM. The AFM-2 was built considering that the spin orientations for all magnetic Mn^{3+} sites are ordered in AFM arrangement. A 2 × 2 × 2 supercell was considered to calculate long-range magnetic interactions. The AFM-3 and AFM-4 models herein were constructed based on the most stable in-plane AFM-2, where AFM-3 corresponds to an in-plane AFM arrangement and out-of-plane FEM configuration, whereas the AFM-4 model is completely ordered in an AFM arrangement with both in-plane and out-of-plane exchange coupling in antiparallel ordering. The exchange coupling constant was computed using the Ising model

$$\hat{H}_{\text{Ising}} = \sum J_{ij} S_{iz} S_{jz} \quad (1)$$

where J_{ij} is the magnetic exchange coupling constant between magnetic neighbors and S_z corresponds to the spin momentum. Next, the (001), (100), (101), (110), (111), (113), and (311) surfaces were considered in order to gain deep insight into the role that the $CuMnO_2$ surfaces plays in the crystal morphology and material properties, as shown in Figure S1.

The surface energy (E_{surf}) was calculated using the equation

$$E_{\text{surf}} = \frac{(E_{\text{slab}} - nE_{\text{bulk}})}{2A} \quad (2)$$

In this case, n is the number of the surface molecular units, E_{bulk} is the total energy of the bulk, E_{slab} is the total energy of the surface slab per molecular unit, and A is the surface area. The equilibrium shape of a crystal and its modulations can be calculated from the Wulff construction, which minimizes the total surface free energy at a fixed volume, providing a simple relationship between the surface energy (E_{surf}) of a (hkl) plane and its distance from the crystallite center in the normal direction.[51] With regard to the magnetic properties for the $CuMnO_2$ morphologies, we considered a recent and innovative method proposed to compute the magnetization index (M) from the calculated spin density (D_μ) index of a given surface.[32,33,52] The latter is related to the magnetic moment (μ_B) per unit cell area (A), while the M values invoke the combination among the contributions of each surface plane to the morphology, $c_{(hkl)}$, and the corresponding D_μ

$$D_\mu = \frac{\mu_B}{A} \quad (3)$$

$$M = \sum c_{(hkl)} \cdot D_\mu^{(hkl)} \quad (4)$$

Electronic integration was performed using a dense 6 × 6 × 6 Monkhorst−Pack[53] k mesh containing 68 k points for the bulk models and 6 × 6 × 1 for the surface models containing 13 k points. The accuracy of the Coulomb and exchange integral calculations was controlled by five thresholds set to 8, 8, 8, 8, and 16. The converge criterion for mono- and bielectronic integrals were set to 10^{-8} Ha, while the root-mean-square (RMS) gradient, RMS displacement, maximum gradient, and maximum displacement were set to 3 × 10^{-4}, 1.2 × 10^{-3}, 4.5 × 10^{-4}, and 1.8 × 10^{-3} au, respectively.

RESULTS AND DISCUSSION

Characterization. The XRD patterns for the $CuMnO_2$ samples are shown in Figure 1. All samples were indexed in a unit cell with a monoclinic structure with $C2/m$ space group (no. 12) in agreement with the letter JCPDS 18-448 and the literature.[16,54] The $CuMnO_2$ material presents a crednerite-type anomalous structure; then formation of this material occurs from the Jahn−Teller distortion due to the shift of the Mn atoms from the octahedral center.[55] The patterns show good intensity, thus being samples with a long-range crystalline structure, but it is noted that the increase in temperature and synthesis time resulted in a better definition of peaks, i.e., increased crystallinity. This phenomenon occurs due to the higher period and higher energy provided at synthesis.

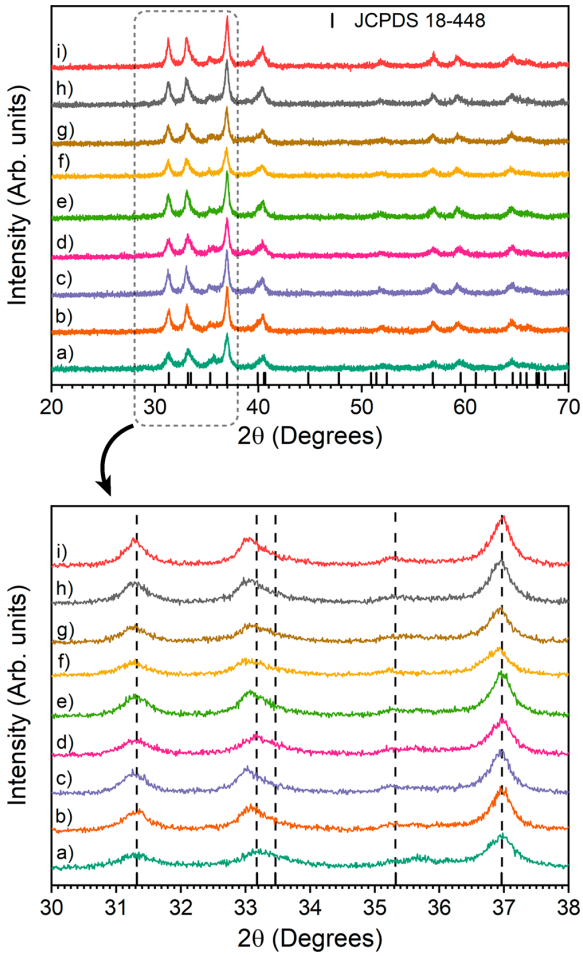

Figure 1. XRD patterns of $CuMnO_2$ samples (a) CM100-1, (b) CM120-1, (c) CM140-1, (d) CM100-5, (e) CM120-5, (f) CM140-5, (g) CM100-10, (h) CM120-10, and (i) CM140-10.

Figure S2 (Supporting Information) and Table S2 summarize the Rietveld refinement results of the XRD patterns. All XRD patterns were indexed as monoclinic cells ($C2/m$) according to ICSD 30379 ($CuMnO_2$). The Obs−Calc lines and reliability parameters χ^2, R_p, and Rf^2 indicated that diffraction patterns of the samples are well adapted. The lattice parameter values found in the literature are in accordance with calculated values (Table S2). For instance, Shukla et al.[20] obtained $CuMnO_2$ by the solid-state method, and lattice parameters results were a = 5.5907(7) Å, b = 2.8808(4) Å, c = 5.8853(7) Å, and β = 103.940(4)°. Moreover, small changes in the lattice parameters among the $CuMnO_2$ samples are noted due to the different temperature and synthesis time.

https://dx.doi.org/10.1021/acs.jpcc.0c00198
J. Phys. Chem. C 2020, 124, 5378−5388

As previously mentioned, the crystalline structure of crednerite $CuMnO_2$ can be decomposed in the 2-fold linear $[CuO_2]$ and 6-fold octahedral $[MnO_6]$ clusters. Figure S3 shows the unit cells of $CuMnO_2$ samples and the Cu−O and Mn−O bond distances. It was generally noted that the increases in temperature and time result in the increased bond distance for Cu−O bonds, while the Mn−O bonds showed irregular distortions.

The FE-SEM images obtained for $CuMnO_2$ samples are shown in Figure 2. The morphology of the particles has

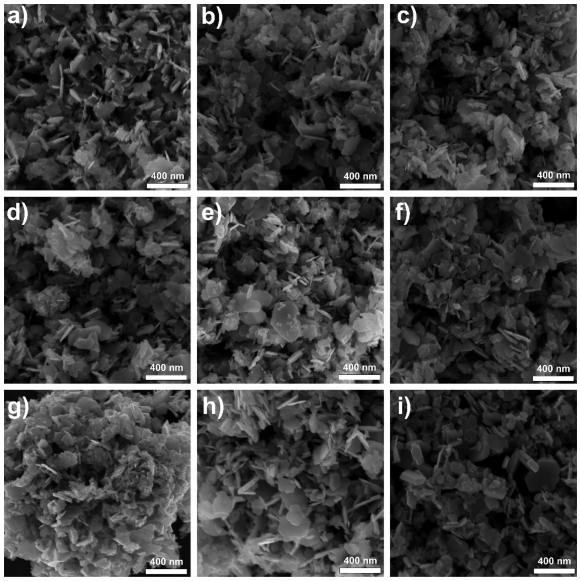

Figure 2. FE-SEM images of $CuMnO_2$ particles, namely, (a) CM100-1, (b) CM120-1, (c) CM140-1, (d) CM100-5, (e) CM120-5, (f) CM140-5, (g) CM100-10, (h) CM120-10, and (i) CM140-10.

nanoplate-like geometry. Moreover, it is noted which particles tend to increase in size with increasing temperature and synthesis time. Also, some CM140-10 particles show nanoplates with hexagonal-like architecture. Xiong et al.[28] and Poienar et al.[12] synthesized $CuMnO_2$ powder by conventional hydrothermal and microwave-assisted hydrothermal methods, respectively, and observed particles with nanoplate-like architecture. On the other hand, Fu et al.[11] synthesized $CuMnO_2$ with special architectures as a function of synthesis temperature. These authors indicate that morphological modulation of the $CuMnO_2$ crystal follows the sequence triangular sheets (140 °C), nanowires (160 °C), hexagonal prisms (180 °C), and octahedrons (over 200 °C).[11] A deep analysis of FE-SEM reported by Fu et al.[11] indicates that hexagonal prisms obtained at 180 °C can be related to the nanoplate-like architecture. In addition, other Cu-based delafossite materials show nanoplate-like morphology[8,56−59] as observed for $CuMnO_2$, confirming that such architecture is characteristic of this material class.

The estimated values for the band-gap energy of $CuMnO_2$ samples are shown in Figure S4. The band-gap energy values (E_{gap}) were estimated using the Kubelka−Munk function[60] followed by the Wood and Tauc method.[61] The band-gap energy is assumed by $\alpha h\nu \propto (h\nu - E_{gap})^{1/p}$,[61] where α is the absorbance, h is Planck's constant, ν is the frequency, and p is indicated for the different kinds of transitions. $CuMnO_2$ is reported with a direct permitted electronic transition,[13] so the results from the $CuMnO_2$ samples were analyzed assuming p = 1/2. The band-gap energy of the $CuMnO_2$ samples reported herein (Figure S4) is close to that obtained by Bellal et al.[13] and Benreguia et al.,[54] which were 1.31 and 1.70 eV, respectively.

Figure S5 shows the isothermal magnetization curves, and Figure 3 presents the isothermal magnetization curves at 5 K and the zero-field-cooled (ZFC) and field-cooled (FC) curves measured between 5 and 300 K for the $CuMnO_2$ samples. In Figure S5 it is possible to observe a paramagnetic state of the samples at 300 K. On the other hand, the curves for the temperature of 5 K clearly evidence the coexistence of the AFM and FM orders, with saturation taking place at magnetic fields above 100 kOe (Figure S5). The coercivity of the samples was found in the range between 5 and 6 kOe, while the remanence was verified between 0.9 and 2.1 emu/g (see the inset on the left in Figure 3). With respect to the remanence, a decrease with increasing temperature is noted for the samples at the same synthesis time.

Regarding the temperature dependence of the magnetization, the FC curves, right panel of Figure 3, show a maximum value at 41 K, while the ZFC curves have an abrupt reduction in this region. This behavior is an indicator of an AFM-like transition, i.e., the material crosses over from a paramagnetic (above 41 K) to an antiferromagnetic state (below 41 K). These observations are in perfect agreement with the experimental results previously reported in the literature.[18−20,22,23]

In addition, all samples have shown distinct values of saturation magnetization, indicating that the magnetic properties of the as-synthesized nanoparticles are connected to the temperature as well as to the synthesis time. This fact is of fundamental importance given that it suggests the role of exposed surface planes on the magnetic anisotropy of $CuMnO_2$ nanoparticles. The main effects associated with such a mechanism are currently under investigation.

DFT Calculations. First, the crystalline structure of $CuMnO_2$ was analyzed considering the theoretical calculations for the unit-cell lattice and M−O (M = Cu, Mn) bond distances. In this case, the lattice parameters of $CuMnO_2$ were calculated as a = 5.690 Å, b = 2.911 Å, c = 5.944 Å, and β = 102.4°, showing good agreement with the experimental evidence reported in Table S2. Regarding the M−O bond distances, the $[CuO_2]$ clusters were formed by Cu−O bond paths of 1.878 Å, while the $[MnO_6]$ clusters have four short (1.942 Å) and two long (2.315 Å) Mn−O bonds in good agreement with experimental data (Figure S3). Therefore, the combination of theoretical and experimental results indicates the existence of Jahn−Teller distortions along the $[MnO_6]$ clusters resulting from the odd number of electrons along the e_g orbital of Mn^{3+} ($3d^4 - t_{2g}^3 e_g^1$).

DFT calculations were carried out on appropriate models to investigate the magnetic ground state of $CuMnO_2$, thus enabling a long-range description. The crystalline structure of $CuMnO_2$ induces two kinds of magnetic exchange coupling constant (J) along the ab plane and c axis, as depicted in Figure 4. The structural arrangement of neighboring magnetic Mn^{3+} cations along the basal (ab) plane induces formation of an isosceles triangular plane with Mn^{3+} cations on the vertices. However, due to the Jahn−Teller distortion generated from the $3d^4$ electron configuration of Mn^{3+} cations, the bond paths

https://dx.doi.org/10.1021/acs.jpcc.0c00198
J. Phys. Chem. C 2020, 124, 5378−5388

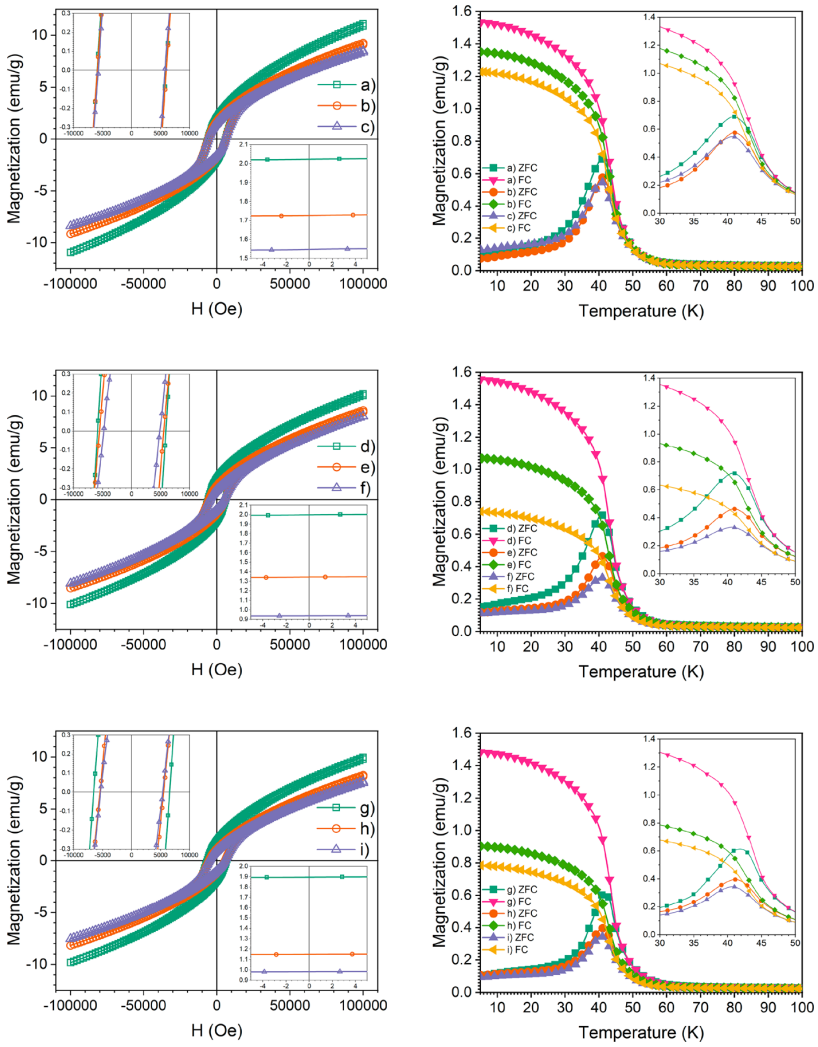

Figure 3. (Left) Magnetization curves at 5 K with inset highlighting the remanence and coercivity of the $CuMnO_2$ samples, namely, (a) CM100-1, (b) CM120-1, (c) CM140-1, (d) CM100-5, (e) CM120-5, (f) CM140-5, (g) CM100-10, (h) CM120-10, and (i) CM140-10. (Right) ZFC and FC curves for the $CuMnO_2$ samples, namely, (a) CM100-1, (b) CM120-1, (c) CM140-1, (d) CM100-5, (e) CM120-5, (f) CM140-5, (g) CM100-10, (h) CM120-10, and (i) CM140-10.

can be divided into two long and one short Mn−O−Mn spin interactions, being denominated J_1 and J_2, respectively.

Nevertheless, the third-neighbor superexchange coupling constant (J_3) along the c axis is mediated along the Mn−O−Cu−O−Mn intermetallic connection, exhibiting a short- and long-part composition. Our calculations were based on the mean value of short and long bond paths in aiming to simplify the evaluation of this magnetic interaction.

Using the Ising model, as presented above (eq 1), the J_1, J_2, and J_3 exchange coupling constants were calculated to be −7.45, −87.07, and −0.21 K, respectively. In addition, the magnetic moment in the Mn^{3+} cation was calculated as 3.62 μ_B, which is in agreement with the high-spin $3d^4$ electronic configuration. In this case, it was noted that all exchange coupling constants are AFM, thereby confirming the long-range antiferromagnetic ground state for $CuMnO_2$. Ushakov et al.[34] also calculated the exchange coupling constant for $CuMnO_2$ using the GGA+U methodology, obtaining values of J_1 = 1.5 K, J_2 = −16.5 K, and J_3 = −0.80 K, with the major differences being attributed to the FM character of long (J_1) Mn−O−Mn exchange coupling. Here, it is important to point out that the exchange coupling constant calculated with the B3LYP formalism shows a similar pattern when compared with the values obtained by the GGA+U formalism differing in the overall magnitude, which can be attributed to treatment of the exchange-correlation effects as previously reported in other theoretical studies.[46,62] However, both results confirm the dominant character of short Mn−O−Mn exchange coupling constants along the basal plane, once the values calculated for the J_2 magnetic interaction were high in comparison to J_1 and J_3, suggesting that this spin interaction generates the overall AFM ground state for $CuMnO_2$.

The main explanation about the dominant effect of the short Mn−O−Mn exchange coupling constant (J_2) can be made based on the Goodenough−Kanamori−Anderson (GKA) rules for the superexchange coupling constant.[63,64] Three main types

https://dx.doi.org/10.1021/acs.jpcc.0c00198
J. Phys. Chem. C 2020, 124, 5378−5388

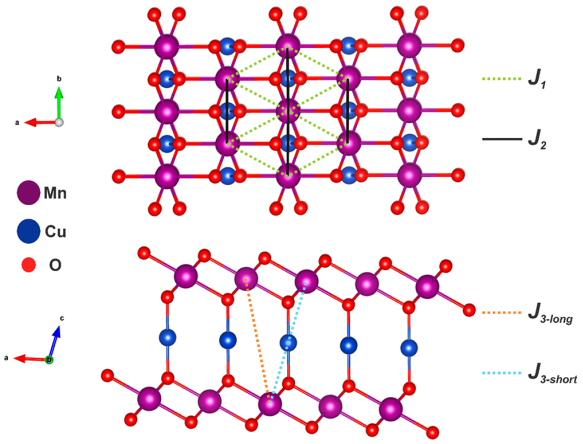

Figure 4. Top- and side-view of crystalline structure for monoclinic $CuMnO_2$ highlighting the existence of distinct exchange coupling constants (J) along the *ab* plane and *c* axis.

of orbital-resolved spin interaction can be described for $CuMnO_2$ along the basal plane. First, the edge-sharing Mn^{3+} can directly interact through the overlap of t_{2g} orbitals which lie on the basal plane. Additionally, the t_{2g} orbitals of neighboring Mn^{3+} can interact by a superexchange coupling constant mediated by oxygen ($2p_z$) orbitals. The last interaction is associated with the coupling of spins mediated by the oxygen-bridge overlap of the t_{2g} and e_g orbitals of neighboring centers. The existence of Jahn−Teller distortions for $CuMnO_2$ along the $[MnO_6]$ clusters induces elongation of two Mn−O−Mn bond interactions along the isosceles triangular basal plane. This fact induces the smallest crystalline orbital overlap along the J_1 exchange coupling for both direct and oxygen-mediated interactions. On the other hand, the short Mn−O−Mn bond paths can be described by a more effective covalent character which increases the extension of atomic orbitals, resulting in the strongest AFM orientation.

In addition, the interlayer exchange coupling constant (J_3) can be associated with the direct overlap between the $3d_{z^2}$ orbitals from Mn^{3+} situated along different layers. However, due to the interlayer distance being too long, the strength of such interaction is very small in comparison to the others, following the principle that the coupling constant from a direct overlap reduces with the distance.

Regarding the electronic structure of the $CuMnO_2$ material, the atomic level description of the main forces which dominate the chemical bond inside the crystalline structure is a key property to understand the most important features associated with this material. Figure 5 shows the band structure profiles and DOS projections for $CuMnO_2$ obtained at the DFT/B3LYP level of theory.

In general, the valence band (VB) is predominantly composed of Cu atomic states hybridized with O valence orbitals. The upper part (maximum) of the valence band (VBM) shows that the energy levels in the vicinity of the Fermi level can be associated with the O−Cu−O bond path oriented along the *c* axis, as this region is mainly attributed to the presence of O ($2p_z$) and Cu ($3d_{z^2}$) orbitals in the same energy range, indicating that the crystalline orbital formed by the combination of both atoms is oriented along the *c* axis. On the other hand, the conduction band (CB) is mainly composed of Mn atomic states combined with 2p orbitals from oxygen. For the conduction band minimum (CBM), both Mn ($3d_{yz}$ and $3d_{xy}$) orbitals dominate the construction of the empty energy levels, especially hybridized by $2p_x$ orbitals of the O atom, with a low contribution of the $2p_y$ and $2p_z$ orbitals. In this case, the 3d orbitals for Mn^{3+} followed the energy level diagram for Jahn−Teller-distorted octahedral environments, showing a crystal field splitting of approximately 0.30 eV, which is expected for such a Mn^{3+} atomic arrangement in $[MnO_6]$ clusters.

Therefore, it was possible to assume that the electronic excitation involving the $CuMnO_2$ electronic structure can be described as an electron-hopping mechanism moving into the Cu−O−Mn intermetallic connection. The calculated E_{gap} was 2.55 eV, being an indirect electronic excitation between Γ and an intermediary point (U) between the A−Z path. In comparison with the experimental results, the obtained band-gap value showed good agreement.

The next step was devoted to clarifying the surface structure for $CuMnO_2$ and their corresponding properties. Table 1 summarizes the main properties calculated for $CuMnO_2$ surfaces at the DFT/B3LYP level of theory. From E_{surf} values, it was observed that the $CuMnO_2$ surfaces have a stability order as (100) > (101) > (111) > (113) > (311) > (110) > (001). In this case, the most stable surface plane corresponded

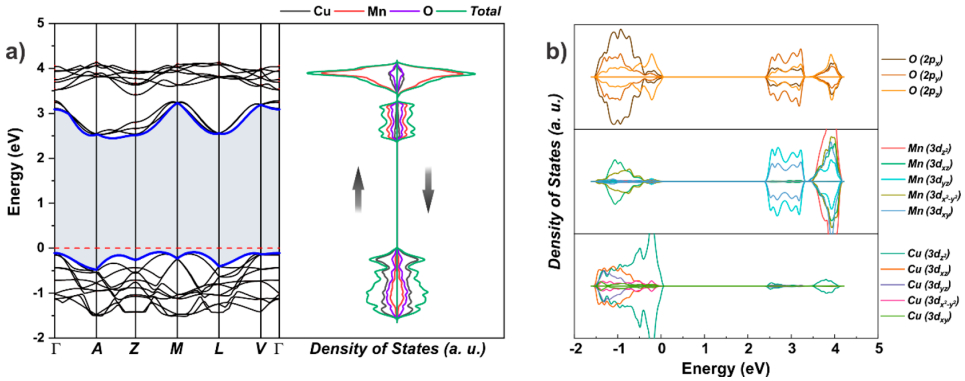

Figure 5. (a) Band structure profiles and atom-resolved DOS profiles for $CuMnO_2$. (b) Orbital-resolved DOS profiles for $CuMnO_2$. Shaded region in the band structure indicates the band-gap region, while blue bands indicate VBM and CBM.

https://dx.doi.org/10.1021/acs.jpcc.0c00198
J. Phys. Chem. C 2020, 124, 5378−5388

Table 1. Surface Energy (E_{surf}), Band Gap (E_{gap}), Area, Magnetic Moment Per Mn Site, and Magnetization Density (D_{μ}) Calculated for $CuMnO_2$ Surfaces

surfaces	E_{surf} (J m^{-2})	E_{gap} (eV)	area (nm^2)	Mn site	moment (μ_B)	D_{μ} (μ_B nm^{-2})
(001)	2.42	metallic	0.083	Mn_{6c}	3.322	0.0
					−3.333	
(100)	0.37	2.03	0.173	Mn_{5c}	3.585	0.0
					−3.585	
(101)	1.10	2.33	0.264	Mn_{5c}	−3.597	13.63
(110)	1.90	metallic	0.186	Mn_{5c}	−3.682	0.0
					3.682	
(111)	1.53	1.98	0.212	Mn_{4c}	−3.555	16.77
(113)	1.58	2.21	0.325	Mn_{4c}	−3.530	10.86
(311)	1.71	2.13	0.333	Mn_{4c}	3.527	10.59

to the (100) plane, which shows pyramidal [MnO_5] clusters as well as linear [CuO_2] clusters. A very interesting observation is associated with the exposed undercoordinated cation of different surfaces. For instance, the (110) and (101) surface planes showed the presence of Mn_{5c} sites similar to the (100), but undercoordinated Cu clusters were not observed for (100), confirming that the dangling bond density modifies the E_{surf} stability from the point of view that additional chemical bonds need to be broken to generate these kinds of surfaces. Following this principle, the (111), (113), and (311) surfaces showed higher E_{surf} values as a function of the increased undercoordinated character of exposed Mn cations. An exception was observed for the (001) surface, as the most unstable plane can be associated with a polar character of the slab associated with exposure of different chemical environments for the upper and lower terminations.

For the electronic structure, the E_{gap} values for the $CuMnO_2$ surfaces reported in Table 1 show similar values to the bulk (2.55 eV). The major differences are associated with the presence of undercoordinated cations along the exposed surfaces, which induce the perturbation on VBM and CBM, as highlighted in Figure S6 (Supporting Information). A special case was observed for both unstable (001) and (110) surfaces, which showed metallic features. The Fermi level for both surface planes crosses the occupied crystalline orbitals for $CuMnO_2$, showing a singular metallic behavior associated with the partially filled $3d^4$ orbitals for Mn^{3+}.

On the other hand, the magnetic moment calculated by the exposed Mn^{3+} sites showed similar values to the bulk (3.62 μ_B), confirming that the spinnet charge of the Mn atoms remained unchanged even in the center of undercoordinated sites.

In magnetic materials, the long-range magnetic order can be dissected on individual contributions from different crystallographic planes.[32] Our calculations indicate that $CuMnO_2$ can be described as a triangular AFM material showing a parallel ferromagnetic arrangement (FEM) to describe the Mn^{3+} spins within the (111) plane, while adjacent planes are coupled antiparallel (AFM). Therefore, it is expected that the (111) plane shows the presence of uncompensated spins as well as for the other planes linked to this one. As presented in Table 1, the (101), (111), (113), and (311) surface planes show a magnetization density associated with the presence of FEM planes along the exposed surfaces. Thus, the (001), (100), and (110) surfaces showed a null total magnetic moment because of the presence of the Mn^{3+} clusters exposed in an AFM arrangement.

The combination of all results previously presented suggests that precise control of exposed surfaces is a key factor to enhance the overall properties of the $CuMnO_2$ material. As morphological modulation is the most effective way to guide the control of exposed surfaces, in this work we investigated the $CuMnO_2$ crystal morphology by employing the Wulff construction,[51] in which the E_{surf} values for each surface determine the final morphology. Therefore, we made a complete set of available morphologies for the $CuMnO_2$ material, as summarized in Figure 6.

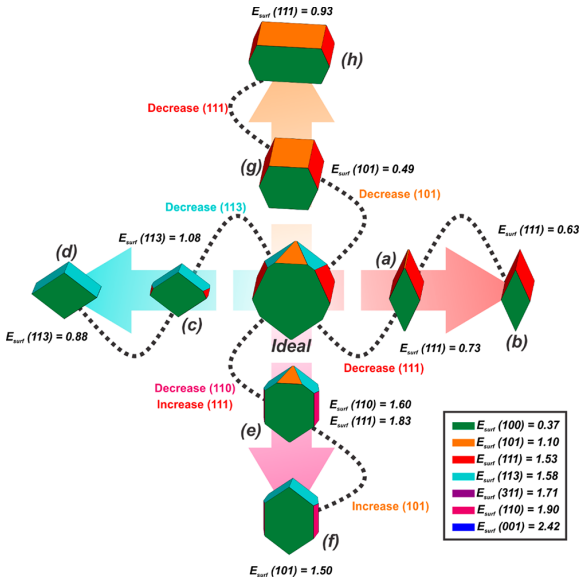

Figure 6. Complete set of available morphologies for $CuMnO_2$ considering the (100), (101), (111), (113), (311), (110), and (001) surfaces.

The vacuum ideal morphology proposed by $CuMnO_2$ exhibited a corner-truncated hexagonal shape enclosing the (100), (111), (101), and (113) surface planes, with the (100) the surface plane presenting the highest contribution due to its E_{surf} value. In addition, a lot of theoretical morphologies (a−f in Figure 6) were proposed by control of the E_{surf} ratio for different surfaces. In the central panel (e−h in Figure 6), it can be seen that hexagonal plate-like morphologies obtained from control of the E_{surf} values for (111), (101), and (110) surfaces are the major differences associated with the nonregular truncation of the hexagonal plate defined by the (100) surface, which remains the most predominant plane along the obtained morphologies.

On the other hand, additional shapes were included in both the left and the right sides (a−d) of the ideal $CuMnO_2$ morphology to describe the major morphological modulations available for this material. In this case, two very similar pseudocubic shapes were found controlling the E_{surf} values for (111) and (113) surface planes, in which the major differences are the enclosed planes on the pseudocubic shape. In the first case, a distorted cubic shape was found controlling the (111) surface energy combining (100) and (111) surface planes. In the opposite direction, a more regular cubic shape was found

https://dx.doi.org/10.1021/acs.jpcc.0c00198
J. Phys. Chem. C 2020, 124, 5378−5388

Table 2. Surface Contribution and Total Magnetization Density (M) Index Calculated for the Different $CuMnO_2$ Morphologies Which Are Shown in Figure 6 (a–h)

	surface contribution (%)							
	(001)	(100)	(101)	(110)	(111)	(113)	(311)	M (μ_B nm^{-2})
ideal	0.0	65.7	7.2	0.0	14.8	0.0	12.3	4.77
a	0.0	50.0	1.4	0.0	48.5	0.0	0.0	8.32
b	0.0	46.0	0.0	0.0	54.0	0.0	0.0	9.06
c	0.0	59.9	0.0	0.0	3.60	36.5	0.0	4.57
d	0.0	54.3	0.0	0.0	0.0	45.7	0.0	4.96
e	0.0	65.0	7.3	10.8	0.0	16.9	0.0	2.83
f	0.0	67.0	0.0	10.6	0.0	22.4	0.0	2.43
g	0.0	51.6	34.6	0.0	13.8	0.0	0.0	7.03
h	0.0	48.1	29.0	0.0	22.9	0.0	0.0	7.79

controlling the E_{surf} for the (113) surface enclosing both the (113) and the (100) surface planes.

Thus, the combination among these morphologies is very important to elucidate a more general picture of the morphological control of $CuMnO_2$. We argue that despite the existence of similar shapes, different surface planes are exposed due to the similarity between the calculated E_{surf} values. From the technological point of view, this behavior is very pronounced because of the modulation in the fundamental properties such as band gap, magnetic moment, and others from the exposed surfaces the different surface planes are intrinsically connected to such properties. More interestingly, the surface properties are different from the same properties simulated in the bulk (Table 1).

The hexagonal plate-like morphology corresponds to the most favorable architecture for $CuMnO_2$ in all cases, as proven by the experimental evidence reported herein and from other experimental results for Cu-based delafossite materials.[8,56−59]

Thus, we calculated the magnetization index (M) for each morphology to confirm the role of morphological modulations on the magnetic properties of $CuMnO_2$, as presented in Table 2.

Careful inspection of Table 2 indicates that the ideal vacuum morphology for $CuMnO_2$ shows a superficial magnetism of 4.77 (μ_B nm^{-2}), with the (100) plane constituting the surface with the highest contribution from the uncompensated spins. In addition, the path connecting morphologies c and d in Figure 6 showed that such morphological modulations did not drastically affect the superficial magnetism, which remains almost constant. On the other hand, the path connecting the e and f morphologies shows the lowest values for M, suggesting that this kind of architecture controls the surface contribution for the overall magnetism, which remains most like the bulk. However, the path connecting the morphologies labeled as a, b, g, and h in Figure 6 shows the highest values of M, proving that precise control of E_{surf} values for the (111) and (101) surfaces are mandatory to enhance the surface ration contribution to increase the overall magnetism of $CuMnO_2$ nanoparticles.

In combining the after-mentioned results, we indicate a high level of correspondence between the theoretically predicted shape and the experimental morphology observed by FE-SEM images, as depicted in Figure 7. Thus, we argue that three morphologies were selected from FE-SEM (Figure 2) due to their agreement with the theoretically predicted shape (Figure 6).

In particular, the control allowed by exposing the (101) and (111) surfaces induced an increase in the number of uncompensated spins along the cited planes, resulting in a substantial increase for the superficial magnetism but mainly for last morphology (M = 7.03). Over time, control of the outcrop of such surfaces finds excellent agreement with the magnetization measurements reported in Figures S3−-S5. Therefore, we argue that is possible to control the overall magnetism in $CuMnO_2$ nanoparticles from single magnetic surfaces exposed on a very specific morphology; therefore, superficial magnetism is a key structure to develop the magnetic property in nanoparticles.

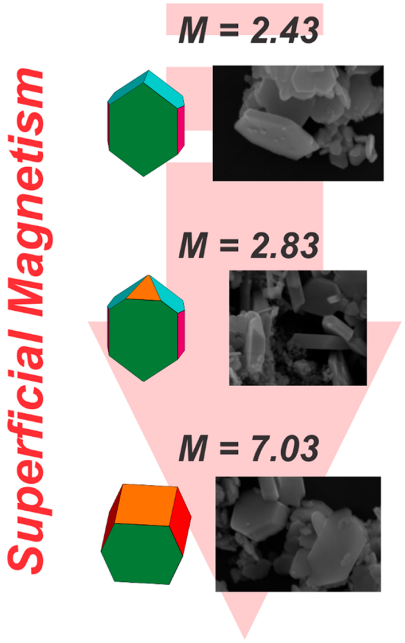

Figure 7. Schematic representation of morphological modulations associated with the increased superficial magnetism of $CuMnO_2$ nanoparticles.

CONCLUSIONS

In this work, a series of crednerite-type $CuMnO_2$ nanoparticles was obtained by a microwave-assisted hydrothermal method, and their fundamental properties were disclosed by experimental and theoretical efforts. Structural characterization indicates that all of the obtained samples exhibit a Jahn−Teller-distorted monoclinic structure. A series of $CuMnO_2$ morphologies was obtained with a nanoplate-like architecture

https://dx.doi.org/10.1021/acs.jpcc.0c00198
J. Phys. Chem. C 2020, 124, 5378−5388

by controlling the synthesis time and temperature. Thus, theoretical analysis was carried out based on the Wulff construction to elucidate this fact, confirming that hexagonal nanoplate-like $CuMnO_2$ morphologies can be obtained by controlling the ratio of the (111), (101), and (110) surface energy values, and showing excellent agreement with experimentally predicted shapes. On the other hand, the superficial magnetism was deeply analyzed focusing on the existence of uncompensated spins along the exposed surface planes of triangular antiferromagnetic $CuMnO_2$. The obtained results clarify the observed magnetizations, indicating that similar hexagonal nanoplate-like $CuMnO_2$ enclosed by different planes showed a distinct magnetization index which came from the singular spin density distribution along the different surfaces. In summary, our study illustrates the great potential of first-principle calculations combined with experimental evidence for developing semiconductors and designing highly efficient $CuMnO_2$ materials with desirable properties.

■ ASSOCIATED CONTENT

Supporting Information

The Supporting Information is available free of charge at https://pubs.acs.org/doi/10.1021/acs.jpcc.0c00198.

Heat treatment temperatures and times utilized to obtain $CuMnO_2$ powders; structural parameters and graphs of Rietveld refinement; theoretical atomics coordinates; orbital-resolved DOS profiles; surfaces models; Wood and Tauc graphs; magnetization curves (PDF)

■ AUTHOR INFORMATION

Corresponding Authors

A. A. G. Santiago − *LSQM, Laboratory of Chemical Synthesis of Materials, Department of Materials Engineering, Federal University of Rio Grande do Norte, UFRN, Natal, Rio Grande do Norte 59078-900, Brazil;* orcid.org/0000-0002-9173-0476; Email: andersonsantiago@ufrn.edu.br

M. R. D. Bomio − *LSQM, Laboratory of Chemical Synthesis of Materials, Department of Materials Engineering, Federal University of Rio Grande do Norte, UFRN, Natal, Rio Grande do Norte 59078-900, Brazil;* orcid.org/0000-0001-9016-4217; Email: mauricio.bomio@ct.ufrn.br

Authors

R. L. Tranquilin − *CDMF-UFSCar, Universidade Federal de São Carlos, São Carlos, São Paulo 13565-905, Brazil*

M. C. Oliveira − *LSQM, Laboratory of Chemical Synthesis of Materials, Department of Materials Engineering, Federal University of Rio Grande do Norte, UFRN, Natal, Rio Grande do Norte 59078-900, Brazil;* orcid.org/0000-0003-3392-7489

R. A. P. Ribeiro − *CDMF-UFSCar, Universidade Federal de São Carlos, São Carlos, São Paulo 13565-905, Brazil;* orcid.org/0000-0002-4128-8296

S. R. de Lazaro − *Departamento de Química, State University of Ponta Grossa, Ponta Grossa, Paraná 84030-000, Brazil;* orcid.org/0000-0001-9753-7936

M. A. Correa − *Departamento de Física, Universidade Federal do Rio Grande do Norte, Natal, Rio Grande do Norte 59078-900, Brazil*

F. Bohn − *Departamento de Física, Universidade Federal do Rio Grande do Norte, Natal, Rio Grande do Norte 59078-900, Brazil*

E. Longo − *CDMF-UFSCar, Universidade Federal de São Carlos, São Carlos, São Paulo 13565-905, Brazil;* orcid.org/0000-0001-8062-7791

F. V. Motta − *LSQM, Laboratory of Chemical Synthesis of Materials, Department of Materials Engineering, Federal University of Rio Grande do Norte, UFRN, Natal, Rio Grande do Norte 59078-900, Brazil*

Complete contact information is available at: https://pubs.acs.org/10.1021/acs.jpcc.0c00198

Author Contributions

All authors equally contributed to this work.

Notes

The authors declare no competing financial interest.

■ ACKNOWLEDGMENTS

The authors gratefully acknowledge financial support from the National Council for Scientific and Technological Development (CNPq), the Coordination for the Improvement of Higher Education Personnel (CAPES; Finance Code 001), FAPESP (2013/07296-2), the Federal University of Rio Grande do Norte (PPGCEM-UFRN), the Federal University of São Carlos, and the State University of Ponta Grossa. A.A.G.S. acknowledges financial support from CNPq (140231/2018-8). M.C.O. acknowledges financial support from PNPD/CAPES (2019/88887.319041). R.A.P.R. acknowledges financial support from CNPq (156176/2018-1).

■ REFERENCES

(1) Amrute, A. P.; Łodziana, Z.; Mondelli, C.; Krumeich, F.; Pérez-Ramírez, J. Solid-State Chemistry of Cuprous Delafossites: Synthesis and Stability Aspects. *Chem. Mater.* **2013**, *25*, 4423−4435.

(2) Du, Z.; Xiong, D.; Verma, S. K.; Liu, B.; Zhao, X.; Liu, L.; Li, H. A Low Temperature Hydrothermal Synthesis of Delafossite $Cucoo_2$ as an Efficient Electrocatalyst for the Oxygen Evolution Reaction in Alkaline Solutions. *Inorg. Chem. Front.* **2018**, *5*, 183−188.

(3) Satish, B.; Srinivasan, R. Soft Chemistry Synthesis and Characterization of Nano P-Type Transparent Semiconducting Delafossite Oxides of Type $A^+B^{3+}O_2$ Where A = Cu; B = Al, Ga, and Cr. *Mater. Today: Proc.* **2018**, *5*, 2401−2411.

(4) Schorne-Pinto, J.; Cassayre, L.; Presmanes, L.; Barnabé, A. Insights on the Stability and Cationic Nonstoichiometry of $CuFeO_2$ Delafossite. *Inorg. Chem.* **2019**, *58*, 6431−6444.

(5) Sullivan, I.; Zoellner, B.; Maggard, P. A. Copper(I)-Based P-Type Oxides for Photoelectrochemical and Photovoltaic Solar Energy Conversion. *Chem. Mater.* **2016**, *28*, 5999−6016.

(6) Toyoda, K.; Hinogami, R.; Miyata, N.; Aizawa, M. Calculated Descriptors of Catalytic Activity for Water Electrolysis Anode: Application to Delafossite Oxides. *J. Phys. Chem. C* **2015**, *119*, 6495−6501.

(7) Wu, Y.; Zhang, J.; Li, L.; Wei, J.; Li, J.; Yang, X.; Yan, C.; Zhou, C.; Zhu, B. Proton Conduction and Fuel Cell Using the CuFe-Oxide Mineral Composite Based on $CuFeO_2$ Structure. *ACS Appl. Energy Mater.* **2018**, *1*, 580−588.

(8) Xiong, D.; Du, Z.; Li, H.; Xu, J.; Li, J.; Zhao, X.; Liu, L. Polyvinylpyrrolidone-Assisted Hydrothermal Synthesis of $CuCoO_2$ Nanoplates with Enhanced Oxygen Evolution Reaction Performance. *ACS Sustainable Chem. Eng.* **2019**, *7*, 1493−1501.

(9) Zhang, L.; Tan, X.; Xiong, D.; Chen, Z.; Xu, S.; Deng, W. Study of the Effect of Synthetic Procedure on Microstructure, Defects and Magnetism of Multiferroic $CuFeO_2$ Ceramics. *Appl. Phys. A: Mater. Sci. Process.* **2018**, *124*, 353.

(10) Zorko, A.; Kokalj, J.; Komelj, M.; Adamopoulos, O.; Luetkens, H.; Arčon, D.; Lappas, A. Magnetic Inhomogeneity on a Triangular Lattice: The Magnetic-Exchange Versus the Elastic Energy and the Role of Disorder. *Sci. Rep.* **2015**, *5*, 9272.
(11) Fu, S.; Li, L.; Jing, Y.; Zhang, Y.; Wang, X.; Fang, S.; Wang, J.; Li, G. Crystal Growth of Bimetallic Oxides $Cumno_2$ with Tailored Valence States for Optimum Electrochemical Energy Storage. *Cryst. Growth Des.* **2018**, *18*, 6107−6116.
(12) Poienar, M.; Banica, R.; Sfirloaga, P.; Ianasi, C.; Mihali, C. V.; Vlazan, P. Microwave-Assisted Hydrothermal Synthesis and Catalytic Activity Study of Crednerite-Type $CuMnO_2$ Materials. *Ceram. Int.* **2018**, *44*, 6157−6161.
(13) Bellal, B.; Hadjarab, B.; Benreguia, N.; Bessekhouad, Y.; Trari, M. Photoelectrochemical Characterization of the Synthetic Crednerite $CuMnO_2$. *J. Appl. Electrochem.* **2011**, *41*, 867−872.
(14) Bessekhouad, Y.; Trari, M.; Doumerc, J. P. $Cumno_2$, a Novel Hydrogen Photoevolution Catalyst. *Int. J. Hydrogen Energy* **2003**, *28*, 43−48.
(15) Kato, S.; Fujimaki, R.; Ogasawara, M.; Wakabayashi, T.; Nakahara, Y.; Nakata, S. Oxygen Storage Capacity of $CuMO_2$ (M = Al, Fe, Mn, Ga) with a Delafossite-Type Structure. *Appl. Catal., B* **2009**, *89*, 183−188.
(16) Wang, L.; Arif, M.; Duan, G.; Chen, S.; Liu, X. A High Performance Quasi-Solid-State Supercapacitor Based on $CuMnO_2$ Nanoparticles. *J. Power Sources* **2017**, *355*, 53−61.
(17) Huang, X.; Ni, C.; Zhao, G.; Irvine, J. T. S. Oxygen Storage Capacity and Thermal Stability of the $CuMnO_2$−CeO_2 Composite System. *J. Mater. Chem. A* **2015**, *3*, 12958−12964.
(18) Kurokawa, A.; Yanoh, T.; Yano, S.; Ichiyanagi, Y. Preparation and Magnetic Properties of Multiferroic $CuMnO_2$ Nanoparticles. *J. Nanosci. Nanotechnol.* **2014**, *14*, 2553−2556.
(19) Shukla, K. K.; et al. Magnetic and Optical Properties of Fe Doped Crednerite $CuMnO_2$. *RSC Adv.* **2015**, *5*, 83504−83511.
(20) Shukla, K. K.; Singh, R.; Kumar, A.; Ghosh, A. K.; Chatterjee, S. Griffith-Like Phase in Crednerite $CuMnO_2$. *Mater. Res. Bull.* **2017**, *91*, 135−139.
(21) Poienar, M.; et al. Substitution Effect on the Interplane Coupling in Crednerite: The $Cu_{1.04}Mn_{0.96}O_2$ Case. *Chem. Mater.* **2011**, *23*, 85−94.
(22) Garlea, V. O.; Savici, A. T.; Jin, R. Tuning the Magnetic Ground State of a Triangular Lattice System $Cu(Mn_{1-x}Cu_x)O_2$. *Phys. Rev. B: Condens. Matter Mater. Phys.* **2011**, *83*, 172407.
(23) Terada, N.; Tsuchiya, Y.; Kitazawa, H.; Osakabe, T.; Metoki, N.; Igawa, N.; Ohoyama, K. Magnetic Correlations and the Influence of Atomic Disorder in Frustrated Isosceles Triangular Lattice Antiferromagnet $CuMnO_2$. *Phys. Rev. B: Condens. Matter Mater. Phys.* **2011**, *84*, 064432.
(24) Trari, M.; Töpfer, J.; Dordor, P.; Grenier, J. C.; Pouchard, M.; Doumerc, J. P. Preparation and Physical Properties of the Solid Solutions $Cu_{1+x}Mn_{1-x}O_2$ ($0 \le x \le 0.2$). *J. Solid State Chem.* **2005**, *178*, 2751−2758.
(25) Chen, H.-Y.; Hsu, D.-J. Characterization of Crednerite-$Cu_{1.1}Mn_{0.9}O_2$ Films Prepared Using Sol−Gel Processing. *Appl. Surf. Sci.* **2014**, *290*, 161−166.
(26) Chen, H.-Y.; Hsu, D.-J. X-Ray Photoelectron Spectroscopy Studies the Cation Valencies and Distributions in Crednerite-$Cu_{1.1}Mn_{0.9}O_2$ Thin Films. *J. Alloys Compd.* **2014**, *598*, 23−26.
(27) Zhang, Q.; Xiong, D.; Li, H.; Xia, D.; Tao, H.; Zhao, X. A Facile Hydrothermal Route to Synthesize Delafossite $CuMnO_2$ Nanocrystals. *J. Mater. Sci.: Mater. Electron.* **2015**, *26*, 10159−10163.
(28) Xiong, D.; Zhang, Q.; Du, Z.; Verma, S. K.; Li, H.; Zhao, X. Low Temperature Hydrothermal Synthesis Mechanism and Thermal Stability of P-Type $CuMnO_2$ Nanocrystals. *New J. Chem.* **2016**, *40*, 6498−6504.
(29) Bahmani, F.; Kazemi, S. H.; Wu, Y.; Liu, L.; Xu, Y.; Lei, Y. $CuMnO_2$-Reduced Graphene Oxide Nanocomposite as a Free-Standing Electrode for High-Performance Supercapacitors. *Chem. Eng. J.* **2019**, *375*, 121966.
(30) Chen, Y.; Chen, T.; Wu, X.; Yang, G. $Cumno_2$ Nanoflakes as Ph-Switchable Catalysts with Multiple Enzyme-Like Activities for Cysteine Detection. *Sens. Actuators, B* **2019**, *279*, 374−384.
(31) Poienar, M.; Martin, C.; Lebedev, O. I.; Maignan, A. Advantage of Low-Temperature Hydrothermal Synthesis to Grow Stoichiometric Crednerite Crystals. *Solid State Sci.* **2018**, *80*, 39−45.
(32) Ribeiro, R. A. P.; de Lazaro, S. R.; Gracia, L.; Longo, E.; Andrés, J. Theoretical Approach for Determining the Relation between the Morphology and Surface Magnetism of Co_3O_4. *J. Magn. Magn. Mater.* **2018**, *453*, 262−267.
(33) Ribeiro, R. A. P.; Lacerda, L. H. S.; Longo, E.; Andrés, J.; de Lazaro, S. R. Towards Enhancing the Magnetic Properties by Morphology Control of $ATiO_3$ (A = Mn, Fe, Ni) Multiferroic Materials. *J. Magn. Magn. Mater.* **2019**, *475*, 544−549.
(34) Ushakov, A. V.; Streltsov, S. V.; Khomskii, D. I. Orbital Structure and Magnetic Ordering in Stoichiometric and Doped Crednerite $CuMnO_2$. *Phys. Rev. B: Condens. Matter Mater. Phys.* **2014**, *89*, 024406.
(35) Huang, M. H.; Naresh, G.; Chen, H.-S. Facet-Dependent Electrical, Photocatalytic, and Optical Properties of Semiconductor Crystals and Their Implications for Applications. *ACS Appl. Mater. Interfaces* **2018**, *10*, 4−15.
(36) Khan, I.; Saeed, K.; Khan, I. Nanoparticles: Properties, Applications and Toxicities. *Arabian J. Chem.* **2019**, *12*, 908.
(37) Jagiello, K.; Chomicz, B.; Avramopoulos, A.; Gajewicz, A.; Mikolajczyk, A.; Bonifassi, P.; Papadopoulos, M. G.; Leszczynski, J.; Puzyn, T. Size-Dependent Electronic Properties of Nanomaterials: How This Novel Class of Nanodescriptors Supposed to Be Calculated? *Struct. Chem.* **2017**, *28*, 635−643.
(38) Andrés, J.; Gracia, L.; Gouveia, A. F.; Ferrer, M. M.; Longo, E. Effects of Surface Stability on the Morphological Transformation of Metals and Metal Oxides as Investigated by First-Principles Calculations. *Nanotechnology* **2015**, *26*, 405703.
(39) Toby, B. Expgui, a Graphical User Interface for GSAS. *J. Appl. Crystallogr.* **2001**, *34*, 210−213.
(40) Rietveld, H. A Profile Refinement Method for Nuclear and Magnetic Structures. *J. Appl. Crystallogr.* **1969**, *2*, 65−71.
(41) Dovesi, R.; Erba, A.; Orlando, R.; Zicovich-Wilson, C. M.; Civalleri, B.; Maschio, L.; Rerat, M.; Casassa, S.; Baima, J.; Salustro, S.; Kirtman, B.; et al. Quantum-Mechanical Condensed Matter Simulations with Crystal. *Wires Comput. Mol. Sci.* **2018**, *8*, e1360.
(42) Towler, M. D.; Allan, N. L.; Harrison, N. M.; Saunders, V. R.; Mackrodt, W. C.; Aprà, E. Ab Initio Study of MnO and NiO. *Phys. Rev. B: Condens. Matter Mater. Phys.* **1994**, *50*, 5041−5054.
(43) Doll, K.; Harrison, N. M. Chlorine Adsorption on the Cu(111) Surface. *Chem. Phys. Lett.* **2000**, *317*, 282−289.
(44) Bredow, T.; Jug, K.; Evarestov, R. A. Electronic and Magnetic Structure of $ScMnO_3$. *Phys. Status Solidi B* **2006**, *243*, R10−R12.
(45) Adamo, C.; Barone, V. Toward Reliable Density Functional Methods without Adjustable Parameters: The PBE0Model. *J. Chem. Phys.* **1999**, *110*, 6158−6170.
(46) Ribeiro, R. A. P.; de Lazaro, S. R.; Pianaro, S. A. Density Functional Theory Applied to Magnetic Materials: Mn_3O_4 at Different Hybrid Functionals. *J. Magn. Magn. Mater.* **2015**, *391*, 166−171.
(47) Eglitis, R. I.; Popov, A. I. Systematic Trends in (001) Surface Ab Initio Calculations of ABO_3 Perovskites. *J. Saudi Chem. Soc.* **2018**, *22*, 459−468.
(48) Eglitis, R. I. Ab Initio Calculations of the Atomic and Electronic Structure of $BaZrO_3$ (111) Surfaces. *Solid State Ionics* **2013**, *230*, 43−47.
(49) Heifets, E.; Kotomin, E. A.; Bagaturyants, A. A.; Maier, J. Ab Initio Study of $BiFeO_3$: Thermodynamic Stability Conditions. *J. Phys. Chem. Lett.* **2015**, *6*, 2847−2851.
(50) Heifets, E.; Kotomin, E. A.; Bagaturyants, A. A.; Maier, J. Thermodynamic Stability of Stoichiometric $LaFeO_3$ and $BiFeO_3$: A Hybrid Dft Study. *Phys. Chem. Chem. Phys.* **2017**, *19*, 3738−3755.

https://dx.doi.org/10.1021/acs.jpcc.0c00198
J. Phys. Chem. C 2020, 124, 5378−5388

(51) Wulff, G. Xxv. Zur Frage Der Geschwindigkeit Des Wachsthums Und Der Auflösung Der Krystallflächen. *Z. Kristallogr. - Cryst. Mater.* **1901**, *34*, 449.
(52) Ribeiro, R. A. P.; Andrés, J.; Longo, E.; Lazaro, S. R. Magnetism and Multiferroic Properties at $MnTiO_3$ Surfaces: A Dft Study. *Appl. Surf. Sci.* **2018**, *452*, 463−472.
(53) Monkhorst, H. J.; Pack, J. D. Special Points for Brillouin-Zone Integrations. *Phys. Rev. B* **1976**, *13*, 5188−5192.
(54) Benreguia, N.; Barnabé, A.; Trari, M. Preparation and Characterization of the Semiconductor $CuMnO_2$ by Sol-Gel Route. *Mater. Sci. Semicond. Process.* **2016**, *56*, 14−19.
(55) Damay, F.; Poienar, M.; Martin, C.; Maignan, A.; Rodriguez-Carvajal, J.; André, G.; Doumerc, J. P. Spin-Lattice Coupling Induced Phase Transition in the S = 2 Frustrated Antiferromagnet $CuMnO_2$. *Phys. Rev. B: Condens. Matter Mater. Phys.* **2009**, *80*, 094410.
(56) Xiong, D.; Zhang, Q.; Verma, S. K.; Bao, X.-Q.; Li, H.; Zhao, X. Crystal Structural, Optical Properties and Mott-Schottky Plots of P-Type Ca Doped $CuFeO_2$ Nanoplates. *Mater. Res. Bull.* **2016**, *83*, 141−147.
(57) Shi, L.; Wang, F.; Wang, Y.; Wang, D.; Zhao, B.; Zhang, L.; Zhao, D.; Shen, D. Photoluminescence and Photocatalytic Properties of Rhombohedral $CuGaO_2$ Nanoplates. *Sci. Rep.* **2016**, *6*, 21135.
(58) Li, Y.; Song, Y.; Jiang, Y.; Hu, M.; Pan, Z.; Xu, X.; Chen, H.; Li, Y.; Hu, L.; Fang, X. Solution-Growth Strategy for Large-Scale "$CuGaO_2$ Nanoplate/ZnS Microsphere" Heterostructure Arrays with Enhanced Uv Adsorption and Optoelectronic Properties. *Adv. Funct. Mater.* **2017**, *27*, 1701066.
(59) Yu, M.; Natu, G.; Ji, Z.; Wu, Y. P-Type Dye-Sensitized Solar Cells Based on Delafossite $CuGaO_2$ Nanoplates with Saturation Photovoltages Exceeding 460 Mv. *J. Phys. Chem. Lett.* **2012**, *3*, 1074−1078.
(60) Tolvaj, L.; Mitsui, K.; Varga, D. Validity Limits of Kubelka−Munk Theory for Drift Spectra of Photodegraded Solid Wood. *Wood Sci. Technol.* **2011**, *45*, 135−146.
(61) Wood, D. L.; Tauc, J. Weak Absorption Tails in Amorphous Semiconductors. *Phys. Rev. B* **1972**, *5*, 3144−3151.
(62) Ribeiro, R. A. P.; de Lazaro, S. R.; Gatti, C. The Role of Exchange−Correlation Functional on the Description of Multiferroic Properties Using Density Functional Theory: The $ATiO_3$ (A = Mn, Fe, Ni) Case Study. *RSC Adv.* **2016**, *6*, 101216−101225.
(63) Goodenough, J. B. An Interpretation of the Magnetic Properties of the Perovskite-Type Mixed Crystals $La_{1-x}Sr_xCoO_{3-\lambda}$. *J. Phys. Chem. Solids* **1958**, *6*, 287−297.
(64) Goodenough, J. B. *Magnetism and the Chemical Bond*; Interscience Publishers: New York, 1963.

https://dx.doi.org/10.1021/acs.jpcc.0c00198
J. Phys. Chem. C 2020, 124, 5378−5388